Characterization of Pt-coated twin paraboloidal laboratory capillary high energy X-ray optics

Seret, Anthony; Kehres, Jan; Gundlach, Carsten; Olsen, Ulrik Lund; Poulsen, Henning Friis; Jensen, Dorte Juul; Cordier, Mark; Stripe, Benjamin; Yun, Wenbing ; Zhang, Yubin

Published in:
Optics Express

Link to article, DOI:
10.1364/OE.499829

Publication date:
2023

Document Version
Publisher's PDF, also known as Version of record

Research Article | Vol. 31, No. 23 / 6 Nov 2023 / Optics Express 38840
Optics EXPRESS

Characterization of Pt-coated twin paraboloidal laboratory capillary high energy X-ray optics

Anthony Seret,[1,*] Jan Kehres,[2] Carsten Gundlach,[2] Ulrik Lund Olsen,[2] Henning Friis Poulsen,[2] Dorte Juul Jensen,[1] Mark Cordier,[3] Benjamin Stripe,[3] Wenbing Yun,[3] and Yubin Zhang[1]

[1]Technical University of Denmark, Department of Civil and Mechanical Engineering, Nils Koppels Allé, Building 404, DK- 2800 Kgs. Lyngby, Denmark
[2]Technical University of Denmark, Department of Physics, Fysikvej, building 307, 2800 Kgs. Lyngby, Denmark
[3]Sigray Inc., 5750 Imhoff Drive, Suite I, Concord, CA 94520, USA
*anthony.seret@oca.eu

Abstract: Novel focusing optics composed of twin paraboloidal capillaries coated with Pt, for laboratory X-ray sources are presented and characterized. The optics are designed to focus the X-rays, resulting in an achromatic focused beam with photon energies up to 40 keV. The performance of the optics under different operational conditions is studied by comparing the energy-photon count spectra of the direct and focused beams. Based on these analyses, the optics gain and efficiency as a function of photon energy are determined. A focal spot of 8.5 µm with a divergence angle of 0.59° is observed. The obtained characteristics are discussed and related to theoretical considerations. Moreover, the suitability and advantages of the present optics for X-ray microdiffraction is demonstrated using polycrystalline aluminium. Finally, possibilities for further developments are suggested.

1. Introduction

It has been demonstrated that by the use of focused X-ray beams the local microstructure, including grain, phase, stress and chemistry within materials can be characterized with high spatial resolution. Well established techniques include X-ray microbeam energy dispersive spectrometers [1], microbeam diffracted/fluorescent spectrometers [2,3] and Laue microdiffraction systems [4–8]. Dedicated X-ray focusing optics with a high efficiency and a small focal spot are beneficial for all these techniques allowing improved spatial resolution and shorter measuring time. Developing such X-ray optics is particularly challenging for laboratory instruments, where the beams from X-ray tubes are divergent and polychromatic, with fluxes many orders of magnitude lower than those from synchrotron sources. Nevertheless, large efforts have been devoted to this endeavour, as instruments in the home laboratory often are more popular than those at synchrotron sources because of the daily access.

The position of the focus depends on the photon energy for chromatic optics like compound refractive lenses [9–11], Fresnel zone plates [12,13] and multilayer Laue lenses [14]. To circumvent this limitation, total reflection is used in optics focusing polychromatic X-rays, like for example Kirkpatrick-Baez mirrors [15,16], nested Kirkpatrick-Baez or Montel mirrors [17,18], microchannel plates [19–21], capillaries [1,22–27], and more elaborate mirrors configurations [28]. In particular, capillaries of two main types, polycapillary [29,30] and monocapillary optics [31], sometimes in combination [32], are more frequently used for laboratory X-ray sources, as manufacturing is relatively easy. Monocapillaries can produce smaller focal spots than polycapillaries [31] enabling both finer spatial resolution and more intense signals. Different

#499829 https://doi.org/10.1364/OE.499829
Journal © 2023 Received 23 Aug 2023; revised 15 Oct 2023; accepted 16 Oct 2023; published 1 Nov 2023

Optics EXPRESS

shapes of mirrors in monocapillaries have been tested, including paraboloidal [1,32–34], tapered [23,24], ellipsoidal [26,32,34–39] and mixed ellipsoidal-tapered [27] profiles. Tapered capillaries typically suffer from shorter capillary exit-to-focus distances than non-tapered optics [23,25,27], which may limit the use of auxiliary equipments such as furnaces and stress rigs. Sub-10 µm focal spots have been obtained using paraboloidal [1,34] and ellipsoidal capillary optics [8,34]. However, existing capillary optics can only focus X-rays with energies lower than 20 keV. Higher energy X-rays are harder to focus as the critical total reflection angle is smaller. Heavy element materials, for example platinum, gold and tungsten, are beneficial for increasing the critical angle, but practically it is difficult to manufacture smooth surfaces with those materials.

The aim of the present work is to characterize new X-ray monocapillary optics that are capable of focusing laboratory polychromatic X-rays with energies above 20 keV, especially in the range 25 keV to 40 keV, which are critical for characterizing large and/or dense materials such as metals. The new optics were manufactured using amorphous borosilicate followed by platinum coating on the surface, to overcome the challenges in manufacturing smooth surfaces with desired shapes using heavy metals. The performances of the novel optics are characterized in detail, including the size of smallest spot of the focused beam (hereafter called focal spot) and the optics efficiency. The potential of the optics is demonstrated by investigation of polycrystalline aluminium. Based on the results, possible further developments of the optics are suggested.

2. Presentation and design principles of the optics

The new optics were designed and manufactured by Sigray. The optics are made up of an amorphous borosilicate body with an external cylindrical shape measuring 4 mm in diameter (see Fig. 1). The interior of the optics consists of two identical paraboloidal reflective surfaces facing each other (see Fig. 2). The designed source-to-optics entrance and optics exit-to-optics focal point distances (the optics focal point also being the focus of the downstream paraboloidal surfaces) are both 30 mm. The optics also comprise an aluminium cap on the left *i.e.* upstream side, which houses an aluminium ring holding a tungsten beamstop. In addition, there is an anodized aluminium holder at the center for safe handling of the optics without touching or grabbing the platinum-coated amorphous borosilicate body (see Figs. 1 and 2).

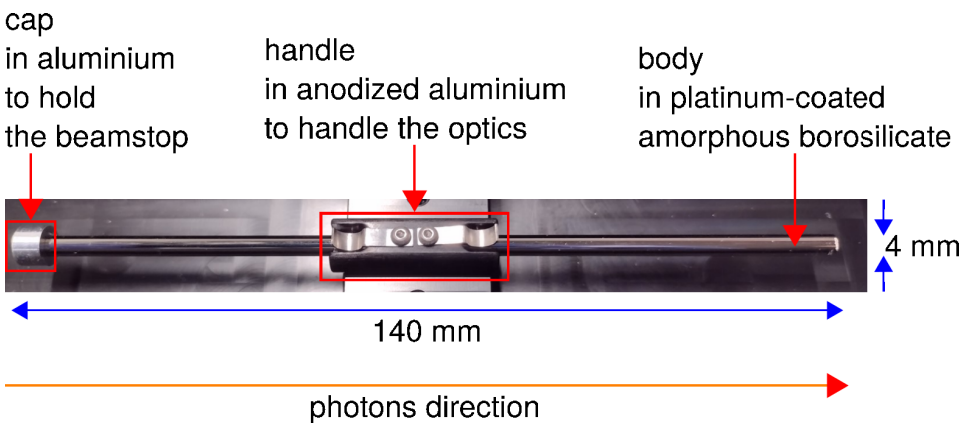

Fig. 1. Photograph of the Sigray twin paraboloidal optics showing the outside cylindrical part of its platinum-coated amorphous borosilicate body, an anodized alumimium black handle (center) and an aluminium cap (left *i.e.* upstream) which houses an aluminium ring holding a tungsten beamstop (both not shown). Photons travel from left to right.

The paraboloidal profile is designed for focusing photons with a point spread function better than 5 µm Gaussian full width at half maximum (FWHM) with a maximum optics efficiency

Optics EXPRESS

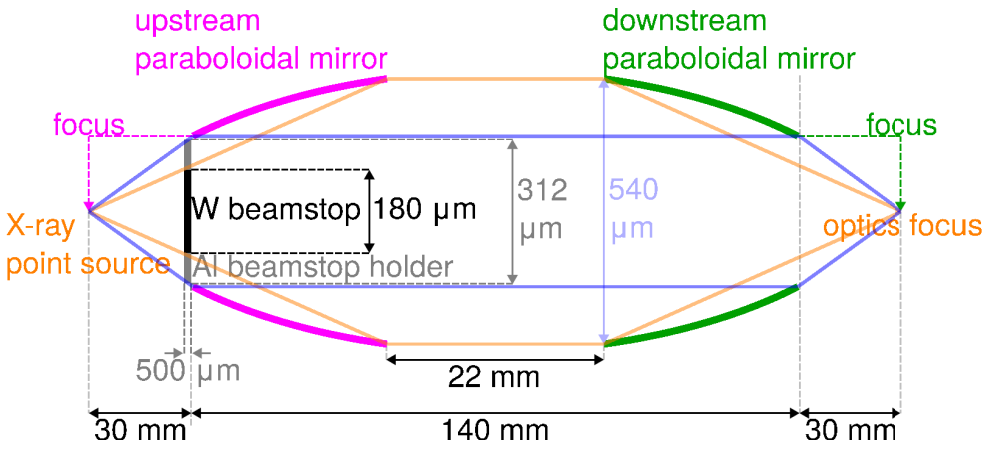

Fig. 2. Main internal parts of the Sigray's optics and principle of the photon path illustrated by semi-transparent blue (largest grazing angle on reflective surfaces) and orange (smallest grazing angle on reflective surfaces and also brushing the beamstop) lines.

for a photon energy of ~32 keV. This energy is chosen to balance the energy range and photon intensities of the focused beam, making it useful for laboratory microdiffraction of typical metals such as aluminium, nickel and iron [40]. The upstream (*i.e.* left in Fig. 2) side is designed to accept photons from the X-ray source through a disk-shaped entrance with a diameter of 312 µm delimited by the border of the upstream mirror. The grazing angle on reflective surfaces is at most 0.149° (blue semi-transparent lines in Fig. 2) and at least 0.087° (orange semi-transparent lines in Fig. 2). The body is coated with a 30 nm-thick layer of platinum which enables the paraboloidal surfaces to reflect X-rays with ideal *i.e.* for perfectly smooth surfaces 80 % and 94 % reflectivity for 30 keV photons at the largest and smallest grazing angles respectively, according to [41].

A cylindrical beamstop (black part in Fig. 2) of diameter 180 µm and thickness 500 µm is placed in this entrance to block centermost photons that would miss the upstream mirror *i.e.* to ensure that all photons entering the optics first hit the upstream mirror; the position and diameter of this beamstop are chosen accordingly. In all cases, the entering photons must cross the (aluminium) holder of the (tungsten) beamstop. When the source point is at the focus of the upstream paraboloidal mirror, all photons entering the optics reflect on the upstream mirror to produce rays parallel to the symmetry revolution axis of the optics, which then reflect on the downstream mirror to intersect at its focus.

Notably, the present optics are the first of their kind for focusing high energy X-rays (> 20 keV) despite utilizing design principles similar to other commercially available Sigray's twin paraboloidal optics for focusing low energy X-rays [34]. The involvement of high energy X-rays impose several manufacturing and physical challenges listed as follows.

1. The (total) reflection angles need to be smaller for an identical reflectivity, which results in a smaller numerical aperture and a smaller entrance diameter, leading to fewer photons entering the optics. It remains to be seen whether the resulting gain is practically useful.

2. A thicker beamstop with a smaller diameter is required to prevent direct beam leakage, which is difficult to manufacture, mount and align, and could introduce some imperfections to the optics.

3. A thicker platinum layer is required, which may lead to a larger surface roughness that reduces the optics' efficiency.

Optics EXPRESS

3. Methods

3.1. Characterization of the optics performance

Characterization of the performace of the optics was carried out in two different setups: (i) an in-house energy-dispersive imaging system (Fig. 3) at the 3D imaging Center of the Technical University of Denmark, to determine the energy-photon count spectra of the direct and focused beams, the optics gain and efficiency as a function of the photon energy; (ii) a customized setup inside a commercial Zeiss Xradia Versa 520 system, with a high-resolution detector to image the focal spot.

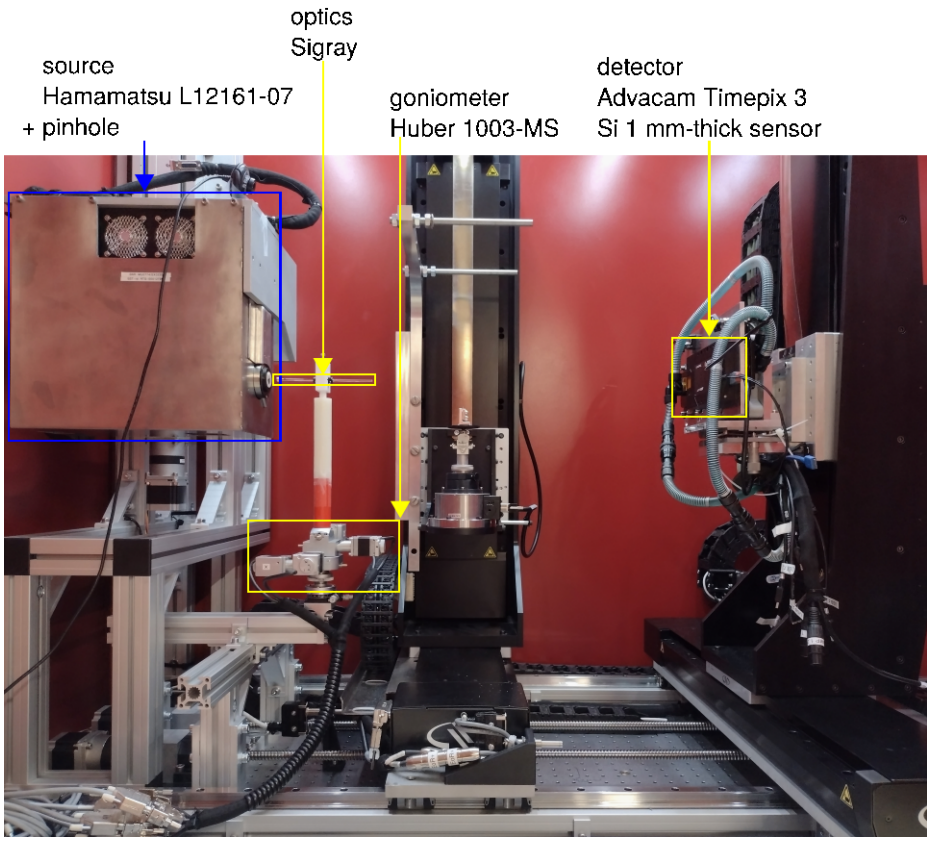

Fig. 3. In-house energy dispersive X-ray imaging setup with highlighted components utilized for the characterization, namely the microfocused X-ray source, goniometer head holding the optics, and the energy dispersive X-ray detector.

In the in-house setup X-rays were produced with a bias of 70 kV at a current of 5 µA by a Hamamatsu L12161-07 [42] source with a tungsten target in small focus mode yielding a source focus spot smaller than 5 µm according to the manufacturer's documentation. The X-ray beam was further collimated by the use of a 400 µm diameter pinhole in a 1 mm-thick tungsten disk to limit background from fluorescence and scattering by the illuminated parts of the setup. The optics was aligned using a fully motorized Huber 1003-MS goniometer head, and photons transmitted through it were registered by an energy-dispersive detector Advacam ADVAPIX TPX3 containing a 1000 µm-thick silicon crystal sensor and a TPX3 readout chip. Detector control and data acquisition were performed using the Pixet software version 1.7.2.857 from Advacam. Fully spectroscopic 2D data were acquired using the build-in Spectral Imaging plugin.

Optics EXPRESS

The maximum detectable number of counts is limited to 5 million per second to allow live time data processing with the Spectral Imaging plugin. Thus a current of 5 µA was used to produce X-rays and stay below this limit.

For both the direct beam and the focused beam, five acquisitions with 2 min acquisition time and 1 keV energy bin width were performed at 50 mm spaced positions along the optical axis, from 363 mm to 563 mm downstream of the source for the direct beam *i.e.* without optics, and from 463 mm to 663 mm downstream of the source *i.e.* 263 mm to 463 mm downstream of the focal spot for the focused beam *i.e.* with optics. Each set of five acquisitions allowed the outer border of the direct and focused beam to be reconstructed, by a least-squares affine regression on the radii (external radii in the case of the ring-shaped images of the focused beam). The affine regression provided the position of the source from direct beam acquisitions and the divergence of the focused beam downstream of the focus (Supplement 1, Fig. S1).

The photon counts of the ten (five for the direct beam and five for the focused beam) acquisitions were each corrected to take into account the quantum efficiency of the detector by considering the following equation:

$$n_t = \frac{n_d}{(1 - \exp(-a \cdot l))} \tag{1}$$

where n_t and n_d are the true and detected numbers of photons per time unit, a is the energy dependent linear absorption coefficient of the sensor material and l the travel length of non-absorbed photons in the sensor. This correction is determined for each pixel taking into account the incident beam angle, which was derived based on the in-house setup geometry. Numerical values for a as a function of photon energy were taken for silicon from [43], and a 1 mm sensor thickness was considered.

The focused beam was studied using the commercial Zeiss Xradia 520 Versa setup, taking advantage of a high-resolution detector. A support structure was added to hold the optics with a manual goniometer Thorlabs PY005/M to align it. X-rays were generated with a Nordson transmission source operated at an electron voltage of 80 kV and a power of 7 W, resulting in a source spot of about 4 µm. The high-resolution detector was a combination of a scintillator, an objective and a charge-coupled-device detector. A x20 objective was used to image the focused beam with an effective pixel size of $\frac{13.4\ \mu m}{20} = 0.67\ \mu m$.

Note that the exact position of the source point inside the source was unknown. At first, the source was moved such that its center was approximately 30 mm from the optics entrance, and the detector moved such that its sensor was placed 200 mm downstream of the source center (thus approximately 30 mm downstream of the optics exit), These two positions were defined as reference positions of the source and detector. Then the source and detector were translated incrementally along the optical axis around their reference positions in steps of 0.5 mm followed by refined steps of 0.1 mm, with the goal of achieving the smallest focal spot. This focal spot was then fitted by a bidimensional Gaussian. Fitted standard deviations were converted to their equivalent Gaussian full widths at half maximum by multiplying them by the factor $2 \cdot \sqrt{2 \cdot \ln 2}$, which were considered the size of the focal spot. The focused beam was also imaged downstream of the focus, where the divergence of the focused beam allowed it to be magnified and thus obtain an image at high resolution.

3.2. Application: diffraction on polycrystalline aluminium

To demonstrate the capability if the optics to yield sufficent signal for practical materials-oriented applications, an X-ray microdiffraction experiment was carried out using the in-house setup, with the optics focusing X-rays on an aluminium polycrystalline sample. The sample has a fully recrystallized microstructure with random crystallographic texture and an average grain size of 50 µm. A rod with a diameter of 700 µm was prepared by electric discharge machining followed by electropolishing using an A2 solution at room temperature.

Optics EXPRESS

X-rays were produced with a source bias of 70 kV at a current of 66 µA, and the detector was an Advacam ADVAPIX TPX3 containing a 1000 µm-thick cadmium-telluride sensor which provided higher sensitivity than the silicon sensor detector. The detector was placed 7 cm downstream of the sample with its center on the optical axis and the acquisition time was set to 30 s. Detector control and data acquisition were again performed using the Pixet software version 1.7.2.857 from Advacam.

To enhance the signal to noise ratio, a 2 mm-thick lead shielding with a 1 mm diameter hole for the passage of the focused beam, was placed between the optics exit and the sample to block the photons that did not go through the optics.

Moreover, a reference image was collected using the same setup and conditions but without the sample. The photon counts of each detector pixel in this reference image were considered as a background and substracted from the photon counts of corresponding detector pixels in the sample diffraction image, to remove this background contribution and to retain only photon counts from the diffraction by the sample.

Table 1 summarizes the link between experimental data and post-processing, setup used and figure(s) using (partially or totally) them.

Table 1. Summary of experimental setups and instruments used for individual figures in this paper.

direct and focused beams as a function of photon energy	in-house setup (Fig. 3)	Fig. 6 Fig. 4 Fig. 7
direct and focused beam at 5 positions to reconstruct their geometries (source position and divergence)	in-house setup (Fig. 3)	Fig. 6 Fig. 7 figure S1
focused beam at high-resolution	Zeiss Xradia Versa 520	Fig. 5(a)
focal spot	Zeiss Xradia Versa 520	Fig. 5(b)
diffraction on aluminium polycrystal	in-house setup (Fig. 3)	Fig. 8

4. Results and discussion

4.1. Geometry of the focused beam

Detector images of the focused beam are shown in Figs. 4 and 5. The ring shape is imaged at a magnified geometry using the divergence of the focused beam downstream of its focus for different photon energies (Fig. 4) and at a high-resolution (Fig. 5(a)). The photon count distributions within the rings are reasonably uniform for X-ray energies in the range 10 keV to 35 keV and the geometry of the focused beam does not depend on the photon energy *i.e.* the focused beam is achromatic (Fig. 4). Nevertheless, some photon count heterogeneity is seen in the high resolution image of the focused beam (Fig. 5(a)), suggesting some minor manufacturing defects of the optics mirrors.

The divergence of the reconstructed focused beam downstream of the focus (Supplement 1, Fig. S1) was calculated as 0.59°, which is very close to the nominal value of 0.60° determined based on the optics and the setup geometry. Figure 5(b) shows the smallest focal spot achieved which was obtained with an acquisition time of 1 s. The size of the focal spot, determined by bidimensional Gaussian fitting, is 8.5 µm.

Optics EXPRESS

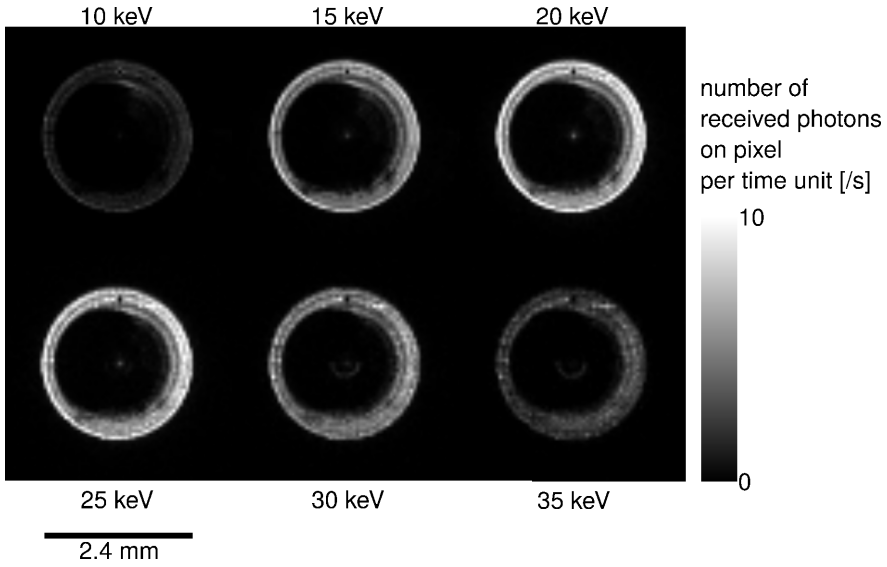

Fig. 4. Focused beam on the detector sensor placed 263 mm downstream of the focus for six photon energy bins of width 1 keV and centers 10, 15, 20, 25, 30 and 35 keV.

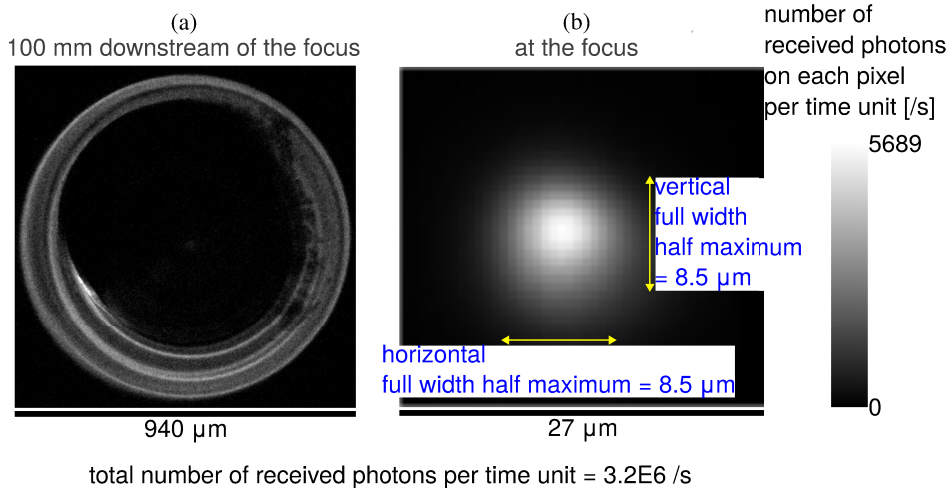

Fig. 5. (a) Image of the focused beam 100 mm downstream of the focus, with an acquisition time of 10 s. (b) Smallest attained focused beam spot, considered as the focal spot, and its colorcode for the number per time unit of received photons on each pixel, with an acquisition time of 1 s. The total number of received photons was 3.2×10^6 s^{-1}.

4.2. Energy-photon count spectra of the direct and focused beams, optics gain and efficiency

The energy-photon count per time unit and per solid angle of the direct and focused beams are presented in Fig. 6. The solid angle was determined (i) for the direct beam, from reconstruction of its geometry by the five detector images measured at positions from 363 mm to 563 mm downstream of the source (section 3.1), and (ii) for the focused beam, by the position and geometry of the optics entrance (disk of diameter 312 µm minus the beamstop disk of diameter 180 µm,

Optics EXPRESS

both at 30 mm from the source side) (section 2, Fig. 2). For the direct beam (red histogram in Fig. 6), two peaks appear representing the superposition of the characteristic tungsten L emission lines and the Bremsstrahlung spectrum. A photon count peak is observed for the focused beam (blue histogram in Fig. 6) at the 26 keV, and overall usable photon count is obtained on the 15 keV to 40 keV photon energy range. Alternating lower and higher photon count densities between neighboring bins are interpreted as an artifact of the acquisition/processing system.

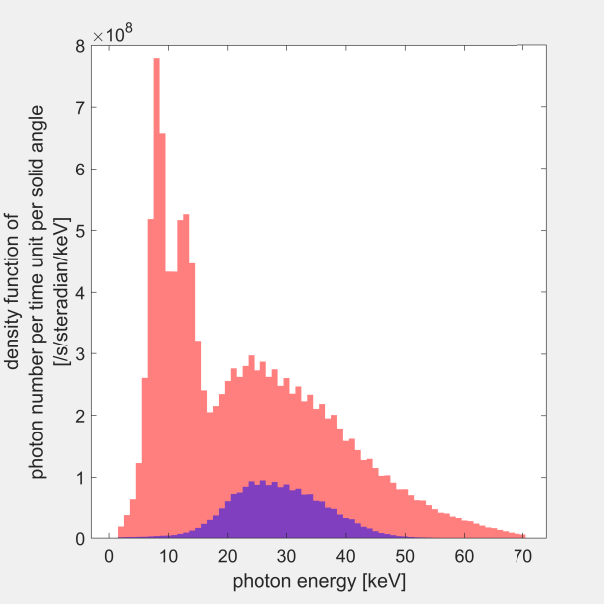

Fig. 6. Spectra energy-photon count per time unit and per solid angle of the direct beam (shown in red) and focused beam (shown in blue). All pixels of the detector were considered to take the full direct and focused beams into account. The acquisition duration was 120 s and photon energy bins have a width of 1 keV.

The theoretical perfect optics gain is defined as the ratio of the number of photons that enter the optics and precisely focus on the working plane (located 200 mm downstream from the source and 30 mm downstream from the optics exit) as the focal spot assuming ideal optics, to the number of photons that would be received on the same working plane within the area defined by the experimentally obtained focal spot but without the optics. Based only on geometrical considerations, the theoretical perfect optics gain is thus independent of the photon energy and equal to the ratio of the solid angle covered by the optics entrance (disk of diameter 312 µm minus the beamstop disk of diameter 180 µm, both at 30 mm from the source side) (section 2, Fig. 2) to the solid angle covered by the experimentally obtained focal spot (disk of diameter 8.5 µm) placed on the working plane. The theoretical perfect optics gain was calculated to be 4.0E4.

Based on the spectral data (Fig. 6), the experimental optics gain as a function of the photon energy was calculated as a function of the photon energy as the ratio of the number of photons per time unit in the focused beam at the focus to the number of photons per time unit in the direct beam that would reach on the working plane the area defined by the experimentally obtained focal spot (disk of diameter 8.5 µm) without the optics.

The optics efficiency was calculated as the ratio of the experimental optics gain over the theoretical perfect optics gain. The optics gain and optics efficiency as a function of the photon energy are shown in Fig. 7. A peak of 32 %, optics efficiency corresponding to an optics gain of 1.3E4 is seen for 30 keV photon energy, which is close to the designed value of 32 keV.

Optics EXPRESS

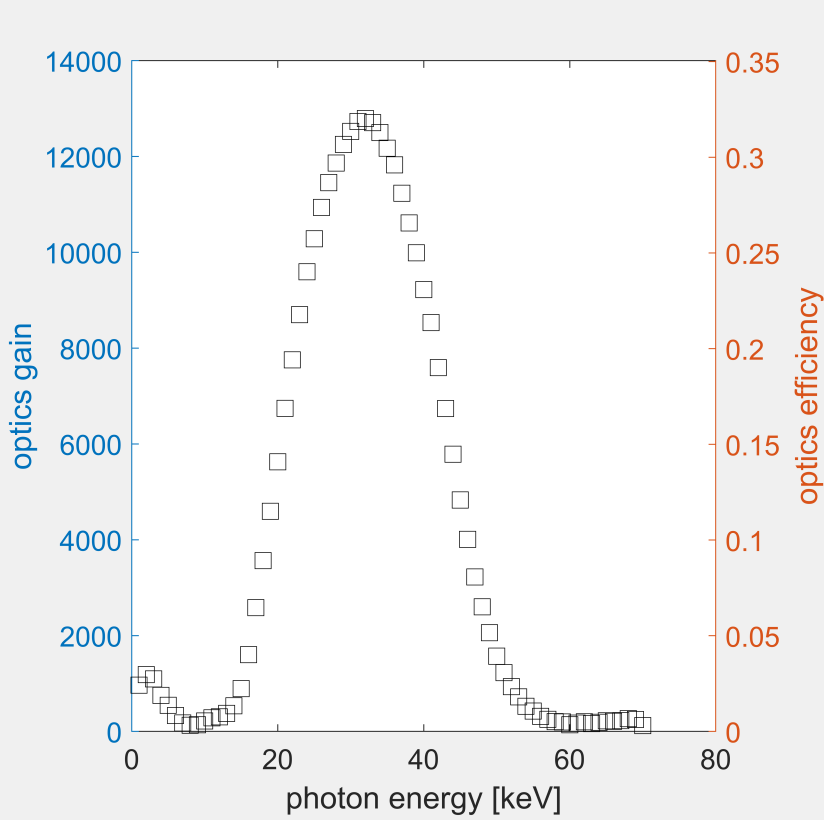

Fig. 7. Optics gain (comparing the number of photons per time unit at the focal spot with and without the optics) and efficiency (comparing the number of photons per time unit exiting and entering the optics) as a function of photon energy.

4.3. Comparison to numerical simulation and theoretical analysis

To understand the optics performances, the experimental results presented in the above two sections are compared to theoretical analyses with regard to the following aspects:

1. the aluminium ring holding the beamstop,
2. the total reflection of photons on the platinum reflective surfaces,
3. deviation from the ideal paraboloidal shape of the platinum reflective surface, which can be decomposed as a short-range contribution corresponding to surface roughness and a long-range contribution corresponding to shape manufacturing error.

The long-range shape of reflective surfaces was characterized and incorporated into a Monte Carlo ray tracing simulation to study its effects on the focal spot. While the detailed measurement process is proprietary, the reflective surfaces profiles of the optics are measured using optical microscopes configured in two orthogonal directions. A source spot size of Gaussian full width at half maximum 4 µm, representative of the Nordson source spot size in the Zeiss Xradia Versa 520 setup, was used.

The simulated focal spot (Supplement 1, Fig. S2) is similar to the experimental one. This result confirms that the long range shape error is the main reason for the focal spot size increase compared

Optics EXPRESS

to the source spot size and the asymmetry of the focal spot. The individual contribution of the long-range mirror shape errors to the focal spot size is estimated as $\sqrt{(8.5\ \mu m)^2 - (4\ \mu m)^2} = 7.5\ \mu m$ assuming that (i) both contributions (source size and shape error of the optics mirrors) to the size of the focal spot are independent and (ii) that the variance (*i.e.* the square of the standard deviation being proportional to the standard deviation of the gaussian law by a factor $2 \cdot \sqrt{2 \cdot \ln 2}$ of the sum of both contributions is equal to the sum of variances.

The effects of other aspects on the optics gain and efficiency were estimated based on theoretical calculations. First, the theoretical transmission efficiency through the (aluminium) ring (holding the beamstop) T_{ring} was calculated using the linear absorption coefficient of aluminium [44] and its 500 µm thickness for different photon energies as shown in (Table 2, second column). The theoretical reflective efficiency on a smooth reflective surface R_{refl} was calculated for both the largest and smallest grazing angles (blue and orange semi-transparent lines in Fig. 2 respectively) on the reflective surface using the equations and values in [45] (Table 2).

Table 2. Theoretical transmission efficiency T_{ring} through the (aluminium) ring (holding the beamstop), theoretical reflective efficiency on one smooth reflective surface R_{refl}, smoothness efficiency E_{smoo} and theoretical optics efficiency $T_{ring} \cdot R_{refl}^2 \cdot E_{smoo}^2$ for both the largest and smallest grazing angles and for X-rays in the photon energy range of 15 keV to 30 keV.

		largest grazing angle			smallest grazing angle		
photon energy [keV]	T_{ring} [%]	R_{refl} [%]	E_{smoo} [%]	$T_{ring} \cdot R_{refl}^2 \cdot E_{smoo}^2$ [%]	R_{refl} [%]	E_{smoo} [%]	$T_{ring} \cdot R_{refl}^2 \cdot E_{smoo}^2$ [%]
15	39	86	90	23	92	94	30
20	64	87	90	40	93	95	50
25	77	86	90	46	94	96	62
30	86	80	85	40	94	96	70

Regarding the roughness of reflective surfaces and its effect on the optics efficiency, it could result from two sources: (i) the surface roughness of the amorphous borosilicate body piloted by surface tension of molten silica, which is estimated to be subnanometric [46], and (ii) the surface roughness of the platinum coating realized by atomic layer deposition, which is evaluated to be subnanometric as well [47,48]. Hence the resulting surface roughness of each of the two reflective surfaces is expected to be less than 2 nm – by considering (i) the position deviation of each of the two (amorphous borosilicate body and platinum coating) surfaces as a random variable and its roughness as its standard deviation, (ii) that both (amorphous borosilicate body and platinum coating) surface position deviations are independent and (iii) that the position deviation of the resulting reflective surface is the sum of both (amorphous borosilicate body and platinum coating) surface position deviations, and that its roughness is thus the square root of the sum of both squared standard deviations (by additivity of variances). Here the theoretical reflective efficiency on a rough reflective surface was calculated considering a 2 nm roughness for both the largest and smallest grazing angles (blue and orange semi-transparent lines in Fig. 2 respectively) using the equations and values reported in [41]. Then the ratio over its counterpart for an ideal *i.e.* smooth reflective surface, called *smoothness efficiency* E_{smoo}, was calculated.

The theoretical optics efficiency, which takes all three aspects into account, was calculated as $T_{ring} \cdot {R_{refl}}^2 \cdot {E_{smoo}}^2$ for both the largest and smallest grazing angles (blue and orange semi-transparent lines in Fig. 2 respectively) (Table 2). All results for the photon energy range 15 keV to 30 keV are listed in Table 2. Overall, the theoretical optics efficiency values (Table 2) are greater than the experimental ones (Fig. 7). Possible reasons are a non-perfect alignment of the beamstop at the entrance and/or non-perfect alignment between both reflective surfaces for instance during the molten borosilicate shaping of the optics body and reflective surfaces, which

Optics EXPRESS

could both block some of the photons and thus reduce the optics efficiency. It could also not be completely ruled out that the roughness of reflective surfaces is larger than 2 nm, as the thickness of the coating is rather thick.

One possibility to increase the optics efficiency could be to replace the 500 µm-thick aluminium ring holding the beamstop by a thinner part of a less absorbing element like graphite. The shape (long-range contribution) and roughness (short-range contribution) of reflective surfaces could be further improved to respectively produce a smaller and more axisymmetrical focal spot and increase the optics transmission efficiency.

4.4. *Application: microdiffraction on polycrystalline aluminium*

A typical diffraction image obtained using the in-house setup with the optics focusing X-rays on an aluminium polycrystalline sample is presented in Fig. 8.

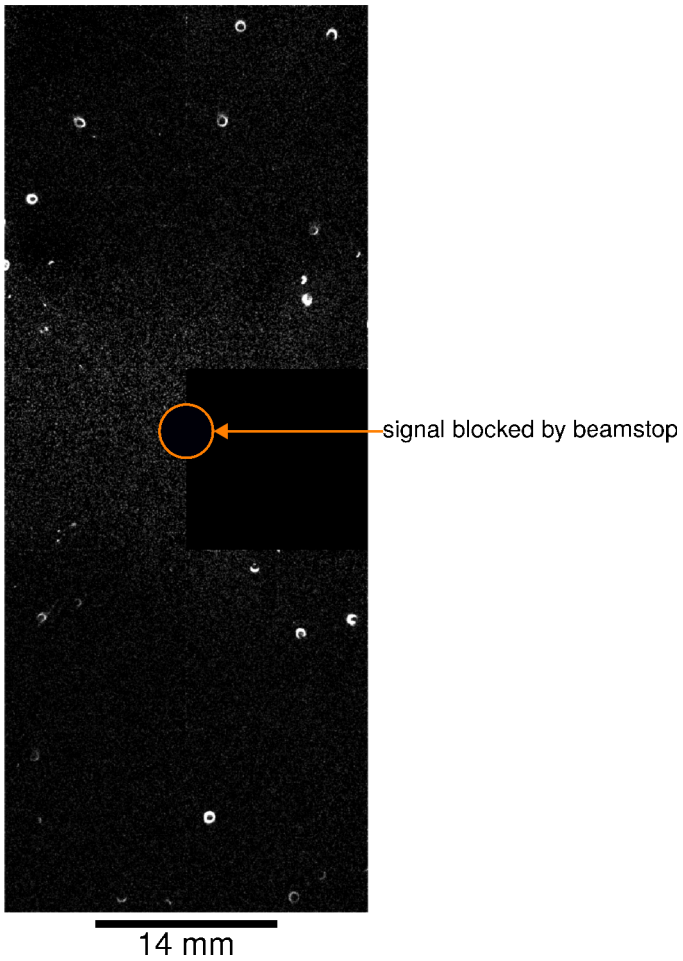

Fig. 8. X-ray diffraction image (after background correction) on a polycrystal aluminium sample (mean crystal size of 50 µm) using the present platinum-coated twin paraboloidal optics. The black area in the central right region is caused by detector faults.

Perfectly visible diffraction spots with a signal-to-noise ratio of 20 to 30 are observed in 30 s of acquisition. A notable feature is the donut shape of diffraction spots, which is interpreted as a result of the divergence of the focused beam and the blockage of the centermost part of the direct

Optics EXPRESS

beam by the beamstop. Some arc-shaped spots are also seen, which suggests that only parts of the focused beam fulfill diffraction condition and/or only parts of the crystals are illuminated by the beam. The latter aspect may provide useful information about the crystal boundary position and crystal shape.

The performance of the present setup is comparable to the most recent home laboratory microdiffraction setup also using photon counting detector [49]. However, the smaller focal spot of the present setup makes it superior in terms of spatial resolution for microdiffraction of metals in home laboratory.

5. Conclusion

The platinum-coated twin paraboloidal laboratory X-ray capillary optics have been characterized to test their performances with regard to the focal spot size, energy bandpass and geometry of the focused beam as a function of photon energy. It is found that the optics (i) are capable of focusing X-rays down to a 8.5 µm Gaussian full width at half maximum focus when a source with spot size of 4 µm is used, (ii) enable an optics gain at the focal point above 8000 in the entire photon energy range 20 keV to 40 keV, and (iii) have a focal length of 30 mm. The divergence of the focused beam is 0.59°. As an additional advantage, the geometry of the focused beam does not depend on the photon energy. In addition, an example of X-ray diffraction pattern on an aluminium polycrystal of mean crystal size 50 µm demonstrates that the presented laboratory optics can be a strong candidate for local and non-destructive analysis of metals with sub-10 µm resolution.

Funding. Villum Fonden (00028354); European Research Council (788567).

Acknowledgments. This work was funded by the Villum Experiment grant, project number 00028354. Dorte Juul Jensen acknowledges the funding from the European Research Council (M4D ERC grant agreement, project number 788567). Authors thank the 3D imaging center at Technical University of Denmark (https://danfix.dtu.dk/) and Xnovotech ApS for allowing to access their equipment.

Disclosures. The authors declare no conflicts of interest.

Data Availability. Data underlying the results presented in this paper are not publicly available at this time but may be obtained from the authors upon reasonable request.

Supplemental document. See Supplement 1 for supporting content.

References

1. Y. Yamamoto and Y. Hosokawa, "Development of an innovative x-ray 5 micro-focused x-ray bean energy-dispersive spectrometer and its applications," Jpn. J. Appl. Phys. **27**(11A), L2203 (1988).
2. N. Yamamoto, "A micro-fluorescent/diffracted x-ray spectrometer with a micro-x-ray beam formed by a fine glass capillary," Rev. Sci. Instrum. **67**(9), 3051–3064 (1996).
3. S. Rouzière, E. Jourdanneau, B. Kasmi, P. Joly, D. Petermann, and P. Albouy, "A laboratory X-ray microbeam for combined X-ray diffraction and fluorescence measurements," J. Appl. Crystallogr. **43**, 1131–1133 (2010).
4. G. E. Ice, J. D. Budai, and J. W. L. Pang, "The race to x-ray microbeam and nanobeam science," Science **334**(6060), 1234–1239 (2011).
5. B. C. Larson, W. Yang, G. Ice, J. D. Budai, and J. Z. Tischler, "Three-dimensional X-ray structural microscopy with submicrometre resolution," Nature **415**(6874), 887–890 (2002).
6. N. Tamura, A. A. MacDowell, R. Spolenak, B. C. Valek, J. C. Bravman, W. L. Brown, R. S. Celestre, H. A. Padmore, B. W. Batterman, and J. R. Patel, "Scanning X-ray microdiffraction with submicrometer white beam for strain/stress and orientation mapping in thin films," J. Synchrotron Rad. **10**(2), 137–143 (2003).
7. P. A. Lynch, N. Tamura, D. Lau, I. Madsen, D. Liang, M. Strohschnieder, and A. W. Stevenson, "Application of white-beam X-ray microdiffraction for the study of mineralogical phase identification in ancient Egyptian pigments," J. Appl. Crystallogr. **40**(6), 1089–1096 (2007).
8. P. A. Lynch, A. W. Stevenson, D. Liang, D. Parry, S. Wilkins, and N. Tamura, "A laboratory based system for laue micro x-ray diffraction," Rev. Sci. Instrum. **78**(2), 023904 (2007).
9. A. Snigirev, V. Kohn, I. Snigirev, H. Chapman, and S. Steenstrup, "A compound refractive lens for focusing high-energy x-rays," Nature **384**(6604), 49–51 (1996).
10. C. Schroer, B. Benner, T. Gü, M. Kuhlmann, C. Zimprich, B. Lengeler, C. Rau, T. Weitkamp, A. Snigirev, I. Snigireva, and J. Appenzeller, "High resolution imaging and lithography with hard x rays using parabolic compound refractive lenses," Rev. Sci. Instrum. **73**(3), 1640–1642 (2002).

Optics EXPRESS

11. F. Stöhr, H. Simons, A. C. Jakobsen, C. H. Nielsen, J. Michael-Lindhard, F. Jensen, H. F. Poulsen, O. Hansen, and J. Hübner, "Injection molded polymeric hard x-ray lenses," Opt. Mater. Express **5**(12), 2804–2811 (2015).
12. C. David, S. Gorelick, S. Rutishauser, J. Krzywinski, J. Vila-Comamala, V. Guzenko, O. Bunk, E. Färm, M. Ritala, M. Cammarata, D. Fritz, R. Barrett, L. Samoylova, J. Gruenert, and H. Sinn, "Nanofocusing of hard x-ray free electron laser pulses using diamond based fresnel zone plates," Sci. Rep. **1**(1), 57 (2011).
13. S. Flenner, A. Kubec, C. David, M. Storm, C. F. Schaber, F. Vollrath, M. Müller, I. Greving, and J. Hagemann, "Hard x-ray nano-holotomography with a fresnel zone plate," Opt. Express **28**(25), 37514–37525 (2020).
14. S. Bajt, M. Prasciolu, H. Fleckenstein, *et al.*, "X-ray focusing with efficient high-na multilayer laue lenses," Light: Sci. Appl. **7**(3), 17162 (2017).
15. P. Kirkpatrick and A. Baez, "Formation of optical images by x-rays," J. Opt. Soc. Am. **38**(9), 766–774 (1948).
16. J. Kim, H.-Y. Kim, J. Park, S. Kim, S. Kim, S. Rah, J. Lim, and K. H. Nam, "Focusing X-ray free-electron laser pulses using Kirkpatrick–Baez mirrors at the NCI hutch of the PAL-XFEL," J. Synchrotron Rad. **25**(1), 289–292 (2018).
17. M. Montel, "X-ray microscopy with catamegonic roof mirrors," X-ray Microsc. Microradiogr. **2**, 177–185 (1957).
18. W. Liu, G. Ice, L. Assoufid, C. Liu, B. Shi, R. Khachatryan, J. Qian, P. Zschack, J. Tischler, and J. Choi, "Achromatic nested kirkpatrick-baez mirror optics for hard x-ray nanofocusing," J. Synchrotron Rad. **18**(4), 575–579 (2011).
19. S. W. Wilkins, A. W. Stevenson, K. A. Nugent, H. Chapman, and S. Steenstrup, "On the concentration, focusing, and collimation of x-rays and neutrons using microchannel plates and configurations of holes," Rev. Sci. Instrum. **60**(6), 1026–1036 (1989).
20. P. Kaaret, P. Geisssbühlers, A. Chen, and E. Glavinas, "X-ray focusing using microchannel plates," Appl. Opt. **31**(34), 7339–7343 (1992).
21. G. Price, A. Brunton, G. Fraser, M. Bavdaz, M. Beijersbergen, J.-P. Boutot, R. Fairbend, S.-O. Flyckt, A. Peacock, and E. Tomaselli, "Hard x-ray imaging with microchannel plate optics," Nucl. Instrum. Methods Phys. Res., Sect. A **490**(1-2), 290–298 (2002).
22. A. Rindby, "Applications of fiber technique in the x-ray region," Nucl. Instrum. Methods Phys. Res., Sect. A **249**(2-3), 536–540 (1986).
23. P. Engström, S. Larsson, A. Rindby, A. Buttkewitz, S. Garbe, G. Gaul, A. Knochel, and F. Lehtenberg, "A submicron synchrotron x-ray beam generated by capillary optics," Nucl. Instrum. Methods Phys. Res., Sect. A **302**(3), 547–552 (1991).
24. D. J. Thiel, D. H. Bilderback, A. Lewis, A. Stern, and T. Rich, "Guiding and concentrating x-rays by using a flexible and hollow-core tapered glass fiber," Appl. Opt. **31**(7), 987–992 (1992).
25. D. Bilderback, S. Hoffman, and D. Thiel, "Nanometer spatial resolution achieved in hard x-ray imaging and laue diffraction experiments," Science **263**(5144), 201–203 (1994).
26. A. Attaelmanan, P. Voglis, A. Rindby, S. Larsson, and P. Engström, "Improved capillary optics applied to microbeam x-ray fluorescence: Resolution and sensitivity," Rev. Sci. Instrum. **66**(1), 24–27 (1995).
27. X. Sun, X. Zhang, Y. Zhu, Y. Wang, H. Shang, F. Zhang, Z. Liu, and T. Sun, "13.1 micrometers hard x-ray focusing by a new type monocapillary x-ray optic designed for common laboratory x-ray source," Nucl. Instrum. Methods Phys. Res., Sect. A **888**, 13–17 (2018).
28. H. Motoyama and H. Mimura, "Two-stage reflective optical system for achromatic 10 nm x-ray focusing," J. Phys. B: At. Mol. Opt. Phys. **48**(24), 244002 (2015).
29. Q. Xiao, I. Ponomarev, A. Kolomitsev, D. Gibson, F. Dilmanian, and E. Nachaliel, "Guiding hard x rays with glass polycapillary fiber," Nucl. Instrum. Methods Phys. Res., Sect. A **347**(1-3), 397–400 (1994).
30. P. J. Schields, D. M. Gibson, W. M. Gibson, N. Gao, H. Huang, and I. Y. Ponomarev, "Overview of polycapillary x-ray optics," Powder Diffr. **17**(2), 70–80 (2002).
31. D. Bilderback, R. Huang, A. Kazimirov, I. Kriksunov, K. Limburg, and E. Fontes, "Monocapillary optics developments and applications," Adv. X-Ray Anal. **46** (2003).
32. X. Sun, Z. Liu, T. Sun, L. Yi, W. Sun, F. Li, B. Jiang, Y. Ma, and X. Ding, "Combined optic system based on polycapillary x-ray optics and single-bounce monocapillary optics for focusing x-rays from a conventional laboratory x-ray source," Nucl. Instrum. Methods Phys. Res., Sect. A **802**, 5–9 (2015).
33. D. X. Balaic, K. A. Nugent, Z. Barnea, R. Garrett, and S. W. Wilkins, "Focusing of X-rays by Total External Reflection from a Paraboloidally Tapered Glass Capillary," J. Synchrotron Rad. **2**(6), 296–299 (1995).
34. X. Zeng, F. Duewer, M. Feser, C. Huang, A. Lyon, A. Tkachuk, and W. Yun, "Ellipsoidal and parabolic glass capillaries as condensers for x-ray microscopes," Appl. Opt. **47**(13), 2376–2381 (2008).
35. R. Huang and D. H. Bilderback, "Single-bounce monocapillaries for focusing synchrotron radiation: modeling, measurements and theoretical limits," J. Synchrotron Rad. **13**(Pt 1), 74–84 (2006).
36. D. Wegrzynek, "Computer microtomography using a laboratory x-ray fluorescence microbeam spectrometer–a feasibility study," X-Ray Spectrom. **30**, 413–418 (2001).
37. A. Bjeoumikhov, N. Langhoff, J. Rabe, and R. Wedell, "A modular system for xrf and xrd applications consisting of a microfocus x-ray source and different capillary optics," X-Ray Spectrom. **33**, 312–316 (2004).
38. F. Gergely, J. Osán, B. K. Szabó, and S. Török, "Analytical performance of a versatile laboratory microscopic x-ray fluorescence system for metal uptake studies on argillaceous rocks," Spectrochim. Acta, Part B **116**, 75–84 (2016).
39. F. Li, Z. guo Liu, and T. xi Sun, "Annular beam high-intensity x-ray diffraction based on an ellipsoidal single-bounce monocapillary," J. Appl. Crystallogr. **49**(2), 627–631 (2016).

Optics EXPRESS

40. A. Lindkvist, H. Fang, D. Juul Jensen, and Y. Zhang, "Optimizing laboratory X-ray diffraction contrast tomography for grain structure characterization of pure iron," J. Appl. Crystallogr. **54**(Pt 1), 99–110 (2021).
41. E. Gullikson, "Mirror reflectivity," https://henke.lbl.gov/optical_constants/layer2.html (2021). Accessed January 18th, 2021.
42. Hamamatsu Photonics, "Microfocus X-ray source L12161-07 - Hamamatsu Photonics," https://www.hamamatsu.com/jp/en/product/type/L12161-07/index.html (2021). Accessed January 18th, 2021.
43. US National Institute of Standards and Technology, Physical Measurements Laboratory, "FFast Physical Reference Database," https://physics.nist.gov/cgi-bin/ffast/ffast.pl?Z=14&Formula=&gtype=5&range=L&lower=1&upper=45&density= (2021). Accessed May 10th, 2021.
44. US National Institute of Standards and Technology, Physical Measurements Laboratory, "FFast Physical Reference Database," https://physics.nist.gov/cgi-bin/ffast/ffast.pl?Z=13&Formula=&gtype=5&range=S&lower=10&upper=26&density= (2021). Accessed May 10th, 2021.
45. E. Gullikson, "Mirror reflectivity," https://henke.lbl.gov/optical_constants/mirror2.html (2021). Accessed January 18th, 2021.
46. K. R. Jensen, P. Fojan, R. L. Jensen, and L. Gurevich, "Surface characterization of coated and uncoated float glass," in *International Summer School on Application of Scanning Probe Microscopy in Life Sciences, Soft Matter and Nanofabrication*, (2013).
47. J. Dendooven, R. K. Ramachandran, K. Devloo-Casier, G. Rampelberg, M. Filez, H. Poelman, G. B. Marin, E. Fonda, and C. Detavernier, "Low-temperature atomic layer deposition of platinum using (methylcyclopentadienyl)trimethylplatinum and ozone," J. Phys. Chem. C **117**(40), 20557–20561 (2013).
48. D. M. Vinsh II, N. Tran, H. Baumgart, and D. Gu, "Mirror reflectivity," http://vmec.server310.com/wp-content/uploads/2017/07/atomic-2009.pdf (2017). Accessed January 18th, 2021.
49. P. A. Lynch, A. W. Stevenson, D. Fox, A. Ghaderi, L. Xie, and M. R. Barnett, "Application of laboratory based laue micro-xrd for generalized grain orientation mapping," SSRN (2019).